Klingler, S., Leven, C., Cirpka, O.A., **Dietrich, P.** (2020):
Anomaly effect-driven optimization of direct-current geoelectric mapping surveys in large areas
J. Appl. Geophys. **176** , art. 104002

http://dx.doi.org/10.1016/j.jappgeo.2020.104002

Title: Anomaly effect-driven optimization of direct-current geoelectric mapping surveys in large areas

Authors:

Stefan Klingler *(corresponding author)*
University Tübingen
GUZ - Center for Geo- and Environmental Sciences,
Schnarrenbergstr. 94-96, 72076 Tübingen, Germany
stefan.klingler@uni-tuebingen.de

Dr. Carsten Leven
University Tübingen
GUZ - Center for Geo- and Environmental Sciences,
Schnarrenbergstr. 94-96, 72076 Tübingen, Germany
carsten.leven-pfister@uni-tuebingen.de

Prof. Dr.-Ing. Olaf A. Cirpka
University Tübingen
GUZ - Center for Geo- and Environmental Sciences,
Schnarrenbergstr. 94-96, 72076 Tübingen, Germany
olaf.cirpka@uni-tuebingen.de

Prof. Dr. Peter Dietrich
University Tübingen
GUZ - Center for Geo- and Environmental Sciences,
Schnarrenbergstr. 94-96, 72076 Tübingen, Germany
and
Helmholtz Centre for Environmental Research GmbH- UFZ,
Department of Monitoring and Exploration Technologies,
Permoserstraße 15, 04318 Leipzig, Germany
peter.dietrich@ufz

Anomaly effect-driven optimization of direct-current geoelectric mapping surveys in large areas

ABSTRACT

In most hydrogeological, geotechnical, archaeological, and other geoscientific applications, we need to understand the lateral extent and connectivity of system-relevant subsurface features. Towards this end, direct-current electric resistivity tomography (ERT) with several 2-D profiles or 3-D grids provides a powerful tool for non-invasive resolution of electrical resistivity anomalies. On the downside, many hours of fieldwork to set up and break down long electrode profiles limit this method to study areas of few thousand square meters, as the workload multiplies with the number of profiles. In many projects, however, determining the extent and connectivity of subsurface anomalies and therefore their potential relevance to the system, may only require the target to be spatially traced instead of fully resolved. We therefore propose geoelectric mapping with a target-specific fixed electrode spacing as an efficient way to trace a resolved resistivity anomaly away from an initial ERT profile, which should be particularly valuable for large study areas. The target-specific electrode spacing is hereby determined by evaluating the effects of the targeted anomaly in the raw data of the preliminary ERT profile. We therefore introduce an anomaly effect applicable to measurements in environments with spatial trends in resistivity distribution. In synthetic simulations, we demonstrate that our approach can efficiently delineate lateral boundaries of resistivity anomalies in ERT data space and we visualize this in pseudosections of anomaly effects. We then apply this method to tracing a gravel-filled paleo-channel in the 8 km^2 Ammer floodplain near Tübingen, Germany and determine a suitable electrode spacing for a subsequent mapping campaign from the ranges of anomaly effects. We traced the paleo-channel over several hundreds of meters away from an initial 550 m long ERT profile within 19 hours, the same time needed to set up, measure, and dismantle the single initial ERT profile. The evaluation of anomaly effects proves to be an efficient tool to detect resistivity anomalies in geoelectric data

and determine suitable electrode spacings for large-scale mapping campaigns. Once identified, anomalies and project-relevant subareas can be the target of more detailed investigations.

KEYWORDS

Geoelectric mapping; anomaly effect; anomaly detection; large-scale site characterization

1 INTRODUCTION

In many geoscientific applications, a thorough identification of the spatial extent and connectivity of subsurface features is important. In hydrogeological studies, for example, we target subsurface units potentially relevant for the overall hydrogeological system behavior, such as the drainage of hillslopes, the connection between surface- and groundwater bodies, or the lateral continuity of preferential groundwater flow paths (Knudby and Carrera, 2005; Trinchero et al., 2008; Renard and Allard, 2013; Wienhöfer and Zehe, 2014; Gonzales Amaya et al., 2016; Uhlemann et al., 2017; Martin et al., 2019). In archaeological studies, the trace and extent of buried anthropogenic structures is relevant to determine their location and geometry as well as their relation and orientation to other structures (Tsokas et al., 2009; Sinha et al., 2013; Moník et al., 2018; Akca et al., 2019; Hauquin and Mourey, 2019). Detecting and mapping these features and structures often represents a fundamental and early project goal and helps defining subareas of interest for more thorough and costly investigations. Especially in large study areas, the preliminary site characterization needs to be time-efficient and inexpensive, yet reliably precise.

Towards this end, a common approach is to combine core drillings and direct-current (DC) geoelectrical surveys in preliminary investigations (Urish, 1983; Bentley and Gharibi, 2004; Chambers et al., 2006; Sinha et al., 2013; Khaki et al., 2016). While core drillings provide a detailed vertical record of the lithology, they are restricted to point locations in the lateral directions. The interpolation of profiles between drilling locations is challenging if the relevant subsurface features have lateral extents smaller than the distance between the boreholes.

Provided that the features of interest show contrasts in electrical resistivity, geoelectric measurements provide spatially continuous data that can be used to fill in gaps between drilling locations and guide the location of new drillings. Commonly, electrical resistivity tomography (ERT) profiles and grids are measured and evaluated with a subsequent inversion of the data set. The inversion result provides a possible subsurface resistivity distribution with depth, lateral boundaries, and thicknesses of geoelectric anomalies. These anomalies may be caused by geological features, cavities, spatial changes in pore fluids, temperature, or moisture content, as well as anthropogenic structures such as archeological artifacts, tunnels, and bunkers.

An anomaly detected in a single 2-D ERT inversion result is typically of relevance to an overall study if it extends perpendicular to the initial ERT profile. Therefore, several studies have used individual 2-D ERT profiles or 3-D grids and subsequent inversion to image the subsurface sedimentary structure (Gonzales Amaya et al., 2016; Martin et al., 2019), the extent of a contaminant plume (Bentley and Gharibi, 2004; Naudet et al., 2004; Maurya et al., 2017), or anthropogenic structures (Chambers et al., 2002; Domenico et al., 2006; Tsokas et al., 2009). In case that only individual 2-D profiles were measured, an anomaly may be interpreted in the 2-D inversion results with subsequent interpolation of its boundaries between the profiles (Dahlin and Loke, 1997; Naudet et al., 2004; Tsokas et al., 2009). Alternatively, as well as for 3-D grid measurements, a full 3-D inversion of the ERT measurements may be applied and interpreted (Chambers et al., 2002; Bentley and Gharibi, 2004; Domenico et al., 2006; Negri et al., 2008; Tsokas et al., 2009; Akca et al., 2019). Regardless of the inversion decision, however, data collection comes with intensive field work and long acquisition times. Even though focused arrays (e.g. Hennig et al., 2008) and multi-channel systems greatly reduce acquisition times, fieldwork continues to consume many hours to set up and later break down electrodes and cables. In our field example discussed below, 20 labor hours per profile were needed. In the characterization of larger study areas, the workload to set up, operate, and dismantle a single ERT profile is multiplied by the number of parallel profiles. As a result, 3-D ERT studies are typically restricted to areas not larger than a few thousand square meters.

As an alternative to multiple full 2-D and 3-D ERT surveys, geoelectric mapping campaigns determine the apparent resistivity of the subsurface with a fixed electrode configuration along profiles (also known as *horizontal profiling* or *constant separation traverses (CST)*) or over 2-D areas. This method was commonly applied to detect and delineate contaminant plumes (Cartwright and McComas, 1968; Warner, 1969; Urish, 1983; Frohlich et al., 1994), sedimentary heterogeneities (Klefstad et al., 1977), and cavities (Worthington and Barker, 1977; Greenfield, 1979; Militzer et al., 1979) before multi-electrode equipment had become popular. Measurements are displayed as a profile or a map of apparent resistivities, and subareas with lateral changes may be targeted with more thorough investigations (Warner, 1969; Kelly, 1976). Such geoelectric mapping with a fixed electrode configuration takes only a fraction of the time needed for the full 2-D ERT survey and especially the time needed to move the equipment from one profile to the next is highly reduced. Hundreds of measurements per day can be taken by field personnel with four mobile electrodes or capacitively coupled towing equipment (Walker and Houser, 2002; Sørensen et al., 2005). With such an approach, an anomaly, once detected, can be traced over large study areas with little effort on acquisition and data evaluation. In addition, a mapping campaign can fill in information between existing, yet distant ERT profiles, vertical electrical soundings (VES), or boreholes to determine the lateral continuity and connectivity of detected features.

The challenge of geoelectric mapping, however, is to find an electrode configuration that is sensitive to the parameter changes in the depth of a target anomaly. Hence, the depth of measurement sensitivity of an electrode configuration represents an important parameter for geoelectric mapping campaigns. Even though this *"depth of measurement sensitivity"* was originally named *"depth of investigation"* (Barker, 1989), this term is nowadays commonly affiliated with depth resolvability of ERT inversions (Oldenburg and Li, 1999). Barker (1989) gives a short summary of studies defining the general depth of measurement sensitivity for different electrode arrays. Typical definitions are based on the assumption of a horizontally layered subsurface. Evjen (1938) defined the depth of measurement sensitivity as the depth with the greatest influence on the measurement (Roy and Apparao, 1971; Roy and Dhar, 1971; Bhattacharya and Sen, 1981). Edwards (1977), in contrast, defined the depth of measurement sensitivity as the depth at which half the signal originates from the volume above and half from below. Both approaches allow practitioners to choose an appropriate electrode spacing in spatial mapping or profiling campaigns according to a specific target depth. The above-mentioned definitions may be used as a rule of thumb, but the electrode configuration applicable to map targeted subsurface features needs to be defined specifically at each site, as the depth of measurement sensitivity strongly depends on the subsurface distribution of electrical resistivity. In contaminant hydrogeological studies, Urish (1983) and Frohlich et al. (1994) therefore first determined a target aquifer layer from a 1-D inversion result of initial vertical electrical soundings. In a second step, the authors compared synthetic vertical soundings with different target layer resistivities to determine the electrode spacing with greatest changes in measured apparent resistivity. This electrode spacing was then used for horizontal profiling in the field to identify the lateral extent of a contaminant plume within the aquifer layer. This approach determines suitable electrode spacings from a preliminary and site specific data set, yet assumes the preliminary vertical soundings to resemble a background resistivity distribution not affected by the contaminant plume. In many studies, however, we might not know locations with a representative background resistivity distribution for preliminary soundings. In addition, this method introduces uncertainty and bias through the inversion and interpretation of the initial vertical soundings. Our present study, by contrast, aims to determine suitable mapping electrode configurations directly from raw data to avoid any unnecessary uncertainty on the lateral anomaly extent.

In this paper, we present an approach to detect geoelectric anomalies in a preliminary ERT data set, determine a site-specific mapping configuration, and trace the spatial extent of a target anomaly over large areas. We first summarize the problems of detectability of resistivity anomalies and review the concept of anomaly effects. We then present an updated anomaly effect for a background resistivity with spatial trends and apply it to anomaly detection and lateral delineation in ERT data space. Finally, we apply this method to two synthetic scenarios as well as a field example from a floodplain in southwestern Germany. Here, we successfully determined a suitable electrode spacing from a preliminary ERT data set and mapped a target anomaly over more than 600,000 m² within hours.

2 BACKGROUND ON DETECTABILITY AND ANOMALY EFFECT

2.1 Detectability of resistivity anomalies

We define a resistivity anomaly as a spatially restricted geometric body in the subsurface with geoelectric properties contrasting the surrounding material. The detectability of a resistivity anomaly strongly depends on the anomaly geometry, its resistivity contrast to the surrounding material, as well as the chosen electrode configuration. In recent years, the detectability of an anomaly was often interpreted as the resolvability of the anomaly in the inversion result. Many studies therefore evaluated the sensitivity matrix or the model resolution matrix to compare different electrode configurations and the resolution of subsurface geometries (Stummer et al., 2004; Day-Lewis, 2005; Wilkinson et al., 2006; Loke et al., 2010; Christiansen and Auken, 2012; Uhlemann et al., 2018). A good resolution is achieved if the true geometry and parameter distribution of the anomaly is reproduced in the inversion result. An inversion, however, introduces a bias by the underlying inversion method and regularization parameters. In contrast to the resolution of a resistivity anomaly, detectability analysis solely focuses on the perturbation of measurements due to a resistivity anomaly. A detectability analysis unbiased by data post-processing may therefore only be possible considering the raw data.

In raw data pseudosections, smaller resistivity anomalies may not perturb the measurements enough to be visually distinguishable from the influence of a heterogeneous background resistivity distribution. In Figure 1, we demonstrate this problem by simulating geoelectric measurements across a synthetic heterogeneous subsurface model using the open-source python libraries of pyGIMLi and pyBERT (Rücker et al., 2006; Rücker et al., 2017). The heterogeneous model represents a horizontally layered subsurface with four layers of 10, 50, 80, and 500 Ωm, respectively (Figure 1a). The four-layered model was inspired by the conceptual geologic understanding of our field site, discussed below. In addition, we created a second model containing a 30 m wide rectangular resistivity anomaly of 1000 Ωm. This anomaly is located between 9 and 15 m depth and could represent a fluvial channel of higher resistive sediments (e.g., gravel, sand). We simulated measurements of a 500 m long Wenner-α ERT profile with an electrode spacing of 1 m centered about the anomaly.

The pseudosections in Figure 1b and c show the simulated measurements for the model without and with the anomaly, respectively. The apparent resistivity ranges in both cases between 10 and 235 Ωm. The two pseudosections are almost identical with a strong increase in apparent resistivity with pseudodepth. In this study, the term “pseudodepth” only identifies the common electrode spacing of measurements plotted on the same level in the pseudosection and does not infer any true depth allocation. An influence from the higher resistive feature can only be inferred from the slightly higher apparent resistivity values in the center. Thus, we can neither determine the presence, nor the lateral extent of the anomaly from the raw data.

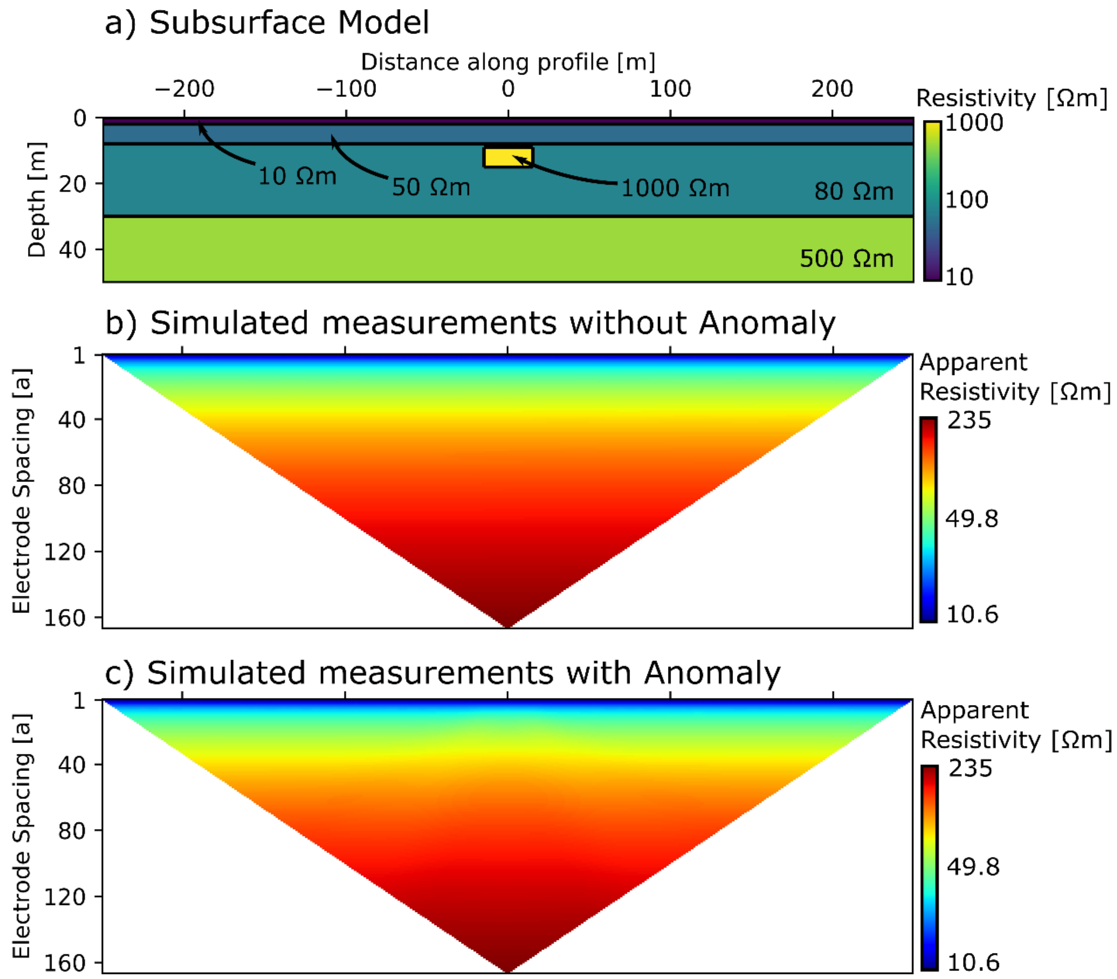

Figure 1: a) Subsurface model used to simulate Wenner-α measurements (a = 1 m) which are displayed in pseudosections for an underlying model b) without an anomaly and c) with a rectangular anomaly of higher resistivity. Ranges of apparent resistivities and qualitative appearance are similar.

1 column with color

2.2 The anomaly effect

Only few studies focused on the detectability analysis based on raw data from geoelectric profile measurements (van Nostrand, 1953; Militzer et al., 1979; Apparao et al., 1992; Szalai et al., 2011; Amini and Ramazi, 2016; Demirel et al., 2018). Early numerical and laboratory studies (van Nostrand, 1953; Carpenter, 1955; Apparao et al., 1992) introduced a resistivity anomaly into a homogeneous half-space and quantified the resulting measurement deviation by

$$AE = \frac{\rho_a}{\rho_1} \quad (1),$$

in which AE is known as anomaly effect, ρ_a denotes the measured apparent resistivity value of a single measurement and ρ_1 is the known resistivity of the homogeneous background, respectively. Militzer et al. (1979) defined the maximum spread of this criterion over a set of measurements as the anomaly effect, which we will address as the *"range of anomaly effects"* (RAE) in the following:

$$RAE = \max\left(\frac{\rho_a}{\rho_1}\right) - \min\left(\frac{\rho_a}{\rho_1}\right) \quad (2).$$

The anomaly effect was used in various studies using different terminology: The *"normalized apparent resistivity"* used to identify deviations in vertical electrical sounding measurements due to terrain effects is identical with the anomaly effect (Sahbi et al., 1997). Also, the *"apparent resistivity anomaly"* used to investigate the sensitivity of geoelectric measurements to fracture geometry and overburden is a scaled simplification of the anomaly effect (Demirel et al., 2018). These authors also define an *"anomaly magnitude"* that is equivalent to the range of anomaly effects.

While the anomaly effect is assigned to each single measurement, the range of anomaly effects is evaluated over a certain subset or the full data set. It was previously used to determine the effectiveness of resistivity measurements (Apparao et al., 1992; Dahlin and Zhou, 2004; Aizebeokhai and Olayinka, 2011; Szalai et al., 2011). This effectiveness is used to compare different arrays and their sensitivity to an anomaly in the subsurface (Dahlin and Zhou, 2004). In studies focusing on the *"depth of detectability"*, the depth of an anomaly is iteratively increased to identify at which depth the range of anomaly effects is smaller than a previously defined error threshold (Szalai et al., 2011). A range of anomaly effects of 10 % serves as a common threshold of detectability (van Nostrand, 1953; Militzer et al., 1979). Measurements with lower anomaly effects are potentially suppressed under conditions with strong noise contamination. Hence, anomalies are not detected in data sets with an overall range of anomaly effects below this threshold.

To our knowledge, only the very few studies cited above considered the anomaly effect as means to evaluate geoelectric raw data. These studies solely focused on the anomaly effect of simple geometries in a homogeneous half-space. Under the condition of a background resistivity with spatial trends (e.g., layering with potentially variable layer thickness), however, the anomaly detection would be inaccurate when taking a homogeneous half-space as reference, as effects caused by the trend in the background will erroneously be attributed to a specific anomaly. Synthetic studies accounting for a spatially variable background normalized the measurements of apparent resistivity perturbed by an anomaly with unperturbed measurements across the same spatially variable background resistivity (Dahlin and Zhou, 2004; Demirel et al., 2018). This, however, only works in synthetic studies, in which the measurements can be simulated with and without the presence of the anomaly. In real-world applications, the subsurface resistivity distribution is likely to show larger spatial variations which dominate the measured apparent resistivity. The challenge thus lies in isolating the effect of an anomaly with contrasting geoelectric properties, indicating a subsurface feature of interest, from the effects of the large-scale trends.

Amini and Ramazi (2016) defined a *"residual resistivity"* to isolate the effect of a resistivity anomaly from a background resistivity distribution and successfully improved inversion results. However, this method uses only a single representative vertical profile to determine a background distribution for the entire dataset and therefore the calculated residual resistivities are biased in case of lateral trends in the background resistivity. To overcome this problem, the lateral variability within a pseudodepth must be considered in the calculation of the background resistivity.

3 ISOLATING THE ANOMALY EFFECT FROM LATERAL TRENDS IN THE BACKGROUND RESISTIVITY

The anomaly effect quantifies the influence of a specific feature with contrasting resistivity on the geoelectric measurements. Its application to realistic data is only possible if the normalization considers lateral variations of the background resistivity distribution. Hence, we consider a vertical sounding curve, as suggested by Amini and Ramazi (2016), as inapplicable for this evaluation.

In this study, we present a method to calculate an anomaly effect in domains with spatially varying resistivity distributions. We first define an anomaly effect normalized to a measurement-specific background apparent resistivity. This background apparent resistivity accounts for lateral and vertical trends. In synthetic simulations, we show suitable methods to calculate the background apparent resistivity from an ERT data set. Finally, we demonstrate the efficient lateral delineation of anomalies in field data. Here, we use the range of anomaly effects to determine the suitable electrode configuration for a subsequent geoelectric mapping.

Rather than comparing the apparent resistivity $\rho_a(i)$ of a specific measurement i to an assumed homogeneous reference resistivity ρ_1, we relate it to an individual background apparent resistivity $\rho_{bg}(i)$, leading to an updated definition of the anomaly effect:

$$AE = \frac{\rho_a(i)}{\rho_{bg}(i)} \qquad (3)$$

with a corresponding range of anomaly effects when considering all locally defined anomaly effects for the same pseudodepth in a profile.

This background apparent resistivity $\rho_{bg}(i)$ is calculated for each pseudodepth individually by taking the median over a certain subset or the full data of the geoelectric profile in this pseudodepth. By this, the background apparent resistivity value has the same electrode configuration factor as the measurement, provided that the topography is flat so that the measurement is not biased by terrain effects. Our definition of the anomaly effect hence yields relative differences within one pseudodepth that can be compared with other pseudodepths.

We present the method for Wenner-α arrays only, but have also successfully applied it to synthetic Schlumberger-array simulations. Both arrays are robust standard configurations available as pre-sets in most geoelectric acquisition equipment. Therefore, both can easily be used to measure an initial representative ERT profile, as well as for the subsequent mapping with four single electrodes. Especially the Wenner-α configuration stands out with low configuration factors and low sensitivity to noise and errors (Dahlin and Zhou, 2004). In addition, the large number of measurements with the same configuration factor provides a solid median background apparent resistivity value during the calculation of the anomaly effect. Other configurations, such as dipole-dipole, might be faster in data acquisition with multi-channel equipment, but are more prone to measurement noise and errors (Zhou and Dahlin, 2003). These configurations also lack the solid median background apparent resistivity for the calculation of anomaly effects, since less measurements share the same configuration factor.

In the following, we present two methods to determine the background apparent resistivity $\rho_{bg}(i)$ for a given pseudodepth from an ERT data set either using the full data set of one pseudodepth or a subsection thereof. Figure 2 shows a profile of apparent resistivities for one pseudodepth, extracted from a full Wenner-α ERT survey. The exemplary data set shows an overall trend of increasing apparent resistivity values from left to right. Higher apparent values were measured in the center of the profile. Between measurement 50 and 100, a local maximum deviates from the shape of the overall curve. Depending on whether this local maximum or the larger-scale hump is addressed as the anomaly, we suggest two approaches of constructing the background apparent resistivity $\rho_{bg}(i)$:

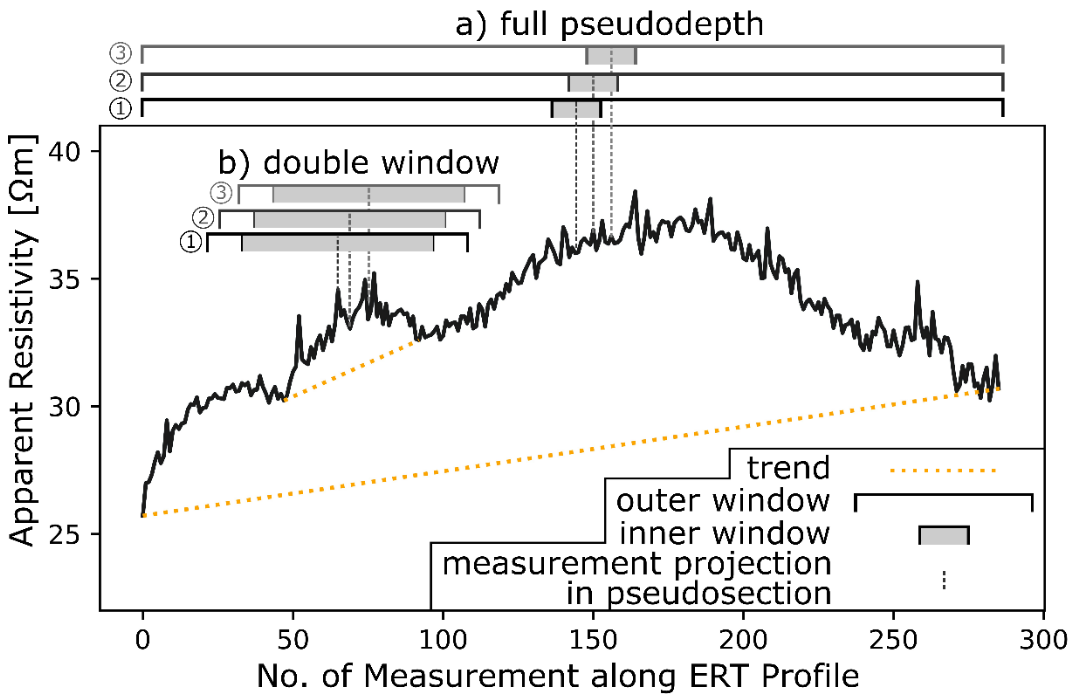

Figure 2: Graphical explanation of two methods to determine a median background apparent resistivity for individual geoelectric measurements. The calculation only considers values in the outer window and excludes those covered by the inner window. The outer window either extends over a) the entire pseudodepth data ("full pseudodepth"), or b) a subsection of it ("double window"). Prior to calculations, the data may be detrended.

1.5 column with color

a.) Determining the background apparent resistivity from the full profile at a given pseudodepth

In this approach, we consider the full-length profile of the measured apparent resistivity in a specific pseudodepth. The individual measurement $\rho_a(i)$ and a certain number of directly neighboring data points are excluded by an inner window to avoid influence of directly neighboring outliers. The width of the inner window is hence data-specific and depends on e.g. the data noise (i.e. higher data noise requires a wider inner window width). With the remaining data, we calculate the background apparent resistivity value by taking the median. For illustration, see the top bars in Figure 2. This approach leads to a slightly varying background value because for each assessment point a different window of excluded data is applied.

However, the difference is small because the median is taken from almost all data at each point. This method is recommended for study areas with only minor expected lateral trends besides the anomaly to be detected.

b.) Determining the background apparent resistivity by double windowing

In study areas with expected strong lateral trends in electrical resistivity, the approach mentioned above would identify these trends as the anomaly. To prevent this, we suggest calculating a local median background apparent resistivity by restricting the analysis to data defined by an outer window (and still excluding the data of the inner window). For illustration, see the bars in the inlet of Figure 2. The inner window size needs to be scaled according to the expected width of the anomaly, to obtain optimal results by effectively suppressing larger background variations along the profile. Both windows are moved along the profile, centered about the location of the measured apparent resistivity $\rho_a(i)$. The measurements on both ends of the profile cannot be used for calculations of the anomaly effect, since no sufficient number of neighbors supports a calculation of the background apparent resistivity. This results in a loss of information of half the outer window size on each side of the profile.

In both methods, we can detrend the data in the outer window prior to the calculation of the anomaly effect. A number of measurements on both ends of the profile is used to determine a linear trend in the data. Details on detrending used in our application are given in Section 3.2.

Figure 3 illustrates the approach for calculating the background apparent resistivity for a scenario with a higher-resistive feature in a laterally homogeneous, layered subsurface, and Figure 4 in a domain where the layer thickness changes laterally. Both scenario models are derived from Figure 1 and consist of four layers with resistivities of 10, 50, 80, and 500 Ωm. The target feature is represented by a 30 m wide rectangular resistivity anomaly of 1000 Ωm. In each scenario we simulated measurements of a 500 m long Wenner-α ERT profile with an electrode spacing of $a = 1$ m centered about the anomaly. The calculated anomaly effects deviate from unity in both negative and positive directions for measured values varying from their individual background apparent resistivity. The results are plotted in pseudosections of anomaly effects to a maximum electrode spacing of 50 a.

3.1 Scenario 1 – Single anomaly in a laterally homogeneous subsurface

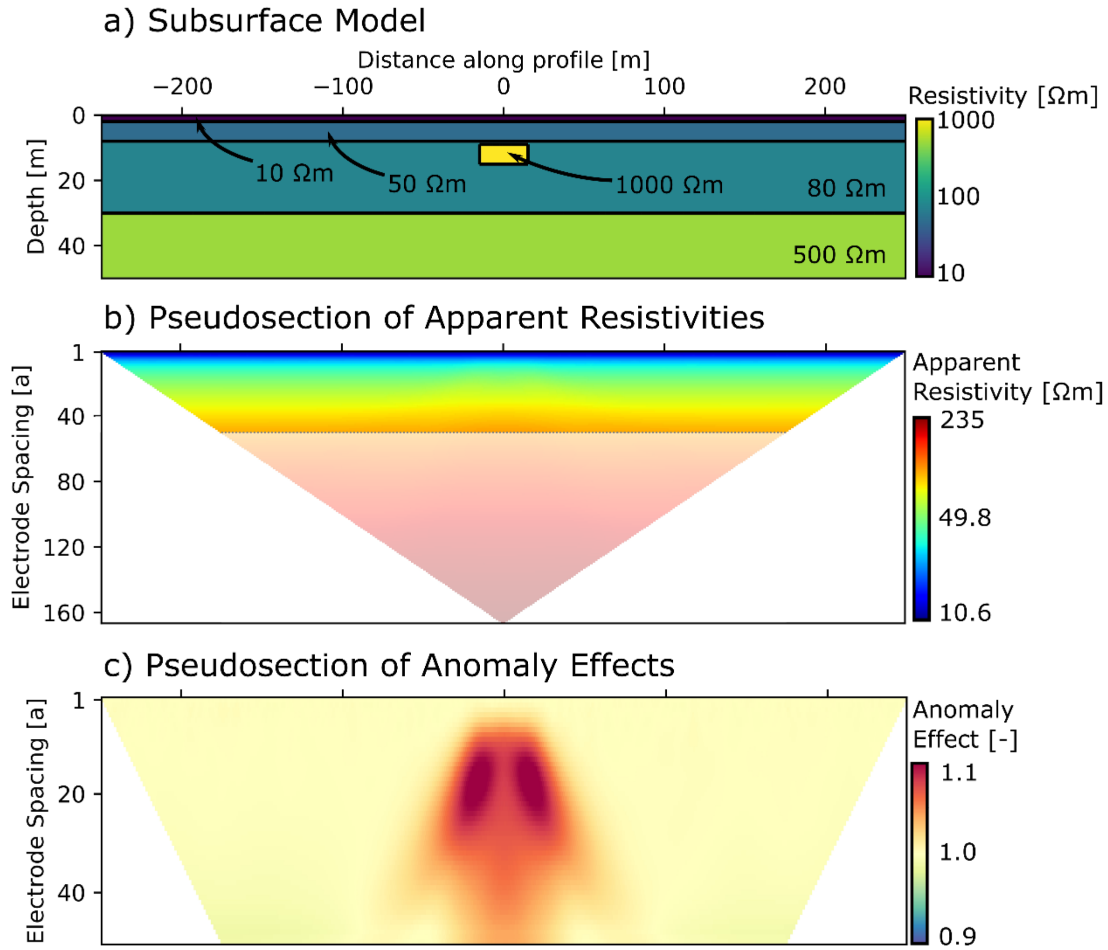

Figure 3: a) Subsurface model, b) resulting pseudosection from synthetic simulations (a = 1 m) comparable to Figure 1, and c) pseudosection of anomaly effects. Electrode spacings > 50 a are faded in b) and not shown in c) since perturbation is negligible for larger electrode spacings. The anomaly effect for each individual measurement is isolated from the influence of the background heterogeneity. The lateral extent of the higher resistive anomaly is obvious.

1 column with color

The first scenario demonstrates the general detectability of an anomaly by calculating the anomaly effects. The resistivity anomaly is six meters thick and located nine meters below the surface (Figure 3a). The simulated apparent resistivity measurements are plotted in a pseudosection and show a gradual increase in apparent resistivity with depth (Figure 3b). No horizontal variation can directly be detected from this, since the downward increase overprints any potential disturbance caused by the resistivity anomaly. We used the median apparent resistivity over the full profile for each pseudodepth to normalize the measured apparent resistivities. The resulting pseudosection of anomaly effects shows high values in the center for electrode spacings of $\approx 17a$, while artifacts spread outside when considering larger electrode spacings (Figure 3c). Small electrode spacings show no anomaly effect ($AE = 1$) over the entire profile. Likewise, measurements in areas to the sides of the anomaly also yield no anomaly effect, which is visualized by the yellow color. These measurements were not perturbed by the deep, central anomaly. Higher anomaly effects are restricted to the center of the pseudosection and shown by warmer colors. The width of the anomaly is slightly overestimated in this pseudosection but can be delineated towards the sides by strong contrasts. A minimum and maximum anomaly effect of 0.972 and 1.110, respectively, results in a range of anomaly effects of 0.137. The positive deviation of 11% from the median background apparent resistivity is hereby larger than the minimum deviation of 10% suggested in earlier studies (van Nostrand, 1953; Militzer et al., 1979) and therefore demonstrates a detectability of the feature even for high measurement errors.

3.2 *Scenario 2 – Single anomaly in a subsurface with lateral trend*

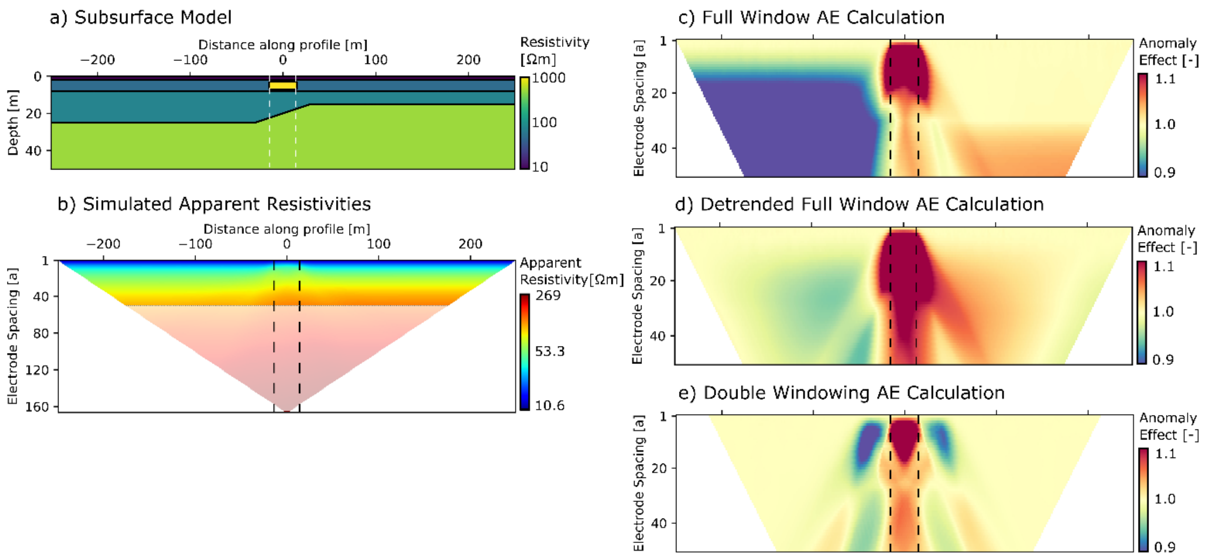

Figure 4: a) Subsurface model and b) resulting pseudosection from synthetic simulations (a = 1 m). Electrode spacings > 50 a are faded in b) and not shown in c), d), and e), since perturbation is negligible for larger electrode spacings. The resulting anomaly effects depend on the method to calculate the background apparent resistivity: c) over the entire pseudodepth, d) over the entire pseudodepth with previous detrending of the data, and e) using the double window approach with an inner window larger than the expected anomaly.

2 columns with color

Figure 4a shows a schematic diagram of the second scenario, in which we changed the depth of the anomaly and considered a lateral change of the third layer: The lower layer boundary shows a steep incline over 60 m in the center of the profile and continues horizontally towards the sides of the model. The highly resistive rectangle is located between three and seven meters depth. Like in scenario 1, the simulated measurements show an increase in apparent resistivity with increasing electrode spacing (Figure 4b). In addition, however, we can observe an increase in the apparent resistivity towards the right for large electrode spacings. This trend is caused by the lateral change in layer thickness. Figure 4c shows the anomaly effect using the full length of the pseudodepth profile as reference. The anomaly can be identified by the highest anomaly effects in the center. Like in scenario 1, the shallowest pseudodepth shows no anomaly effect ($AE = 1$). For larger electrode spacings, and thus larger pseudodepths, the left side is dominated by anomaly effects of $AE < 1$, while the right side shows anomaly effects of $AE \geq 1$. The changing layer thickness leads to a pattern of anomaly effects for electrode spacings > 10 a. Higher apparent resistivities on the right side increase the overall median background apparent resistivity. Consequently, the calculated anomaly effects on the left side are smaller than unity, whereas for electrode spacings larger than 30 a, the anomaly effects on the right-hand side are significantly larger than unity. Nonetheless, the anomaly can be detected, even though with a slightly overestimated width. To improve this result, we detrended the data prior to the calculation of the anomaly effects. We determined the trend with a linear interpolation between the average values of the outermost 10 % of data points on each end of the profile. Subsequently, we removed the trend from the apparent resistivities for the entire profile at each pseudodepth and calculated the anomaly effects from the detrended data (Figure 4d). The anomaly effects on both sides of the central anomaly are damped as the general trend caused by the change in layer thickness is removed. While this method is better in locating the anomaly, it still contains artifacts, and the width of the anomaly is slightly overestimated.

The overall lateral trend in apparent resistivity is visible in the pseudosection of raw measurements shown in Figure 4b. Obviously, the background apparent resistivity for a given pseudodepth is not constant over the entire profile. By applying the double-window method in the calculation of the local background apparent resistivity at a given point, we obtained a better focused anomaly effect (Figure 4e). The width of the outer and inner window is defined based on the expected anomaly width. For field data, this requires a general understanding of expectable features. For this synthetic scenario with known anomaly width, however, we defined a 71 electrodes wide outer window over which the moving median of apparent resistivity was calculated. The inner window was set to 41 electrodes to span wider than the width of the anomaly and hence to avoid strong influences from variations close to the central measurement $\rho_a(i)$. The measurements solely included in the outer window were linearly detrended before we calculated the local background apparent resistivity. This way we isolated the anomaly effect of the rectangular feature from the effects caused by the trend of the layer thickness. We could also determine the width of the anomaly quite well. Artifacts towards the sides and diagonally towards larger electrode spacings do not lower the detectability of the feature, but rather help to delineate the geometry boundary. A loss of data on each side needs to be accepted due to the width of the outer window.

3.3 Comparison and discussion of synthetic scenarios

The synthetic scenarios demonstrate the usefulness of the anomaly effect in detecting subsurface features under consideration of lateral trends in the background resistivity distribution. We can detect and display the anomaly in a pseudosection of anomaly effects. Therein, we identify areas of relative homogeneity by laterally constant anomaly effects of $\approx$1. Areas with strong anomaly effects show similar lateral extents as the features introduced in the initial subsurface model. No prior knowledge on the subsurface resistivity distribution is needed. However, a basic understanding of the potential subsurface architecture is helpful to choose a suitable method to determine the background resistivity value. In addition, the window sizes need to be defined in the double-window method so that the inner window is larger than the expected size of the feature to be detected. In general, the calculation over the full length of the profile for a given pseudodepth is suitable for any single anomaly in an otherwise laterally relatively homogeneous subsurface. As demonstrated in scenario 2, the double-window approach suppresses strong background trends and allows a precise detection of anomaly boundaries even in laterally variable cases. Overall the proposed anomaly effect shows great potential in the lateral delineation of anomalies. However, the pseudosection should still be viewed with caution, as any interpretation on vertical extents and parameter values is inaccurate, comparable to the information in regular pseudosections of raw data. A more probable depth allocation and parameter distribution can only be achieved by inversion of the ERT data. If a full ERT survey, including multiple electrode spacings, has already been obtained, inversion would be the most appropriate way of analyzing the data. As we will show in the following, however, the anomaly detection by directly analyzing the apparent resistivities can guide setting up a geoelectric mapping campaign with fixed electrode spacing, which can be performed much quicker than a full 3-D ERT survey.

4 EVALUATION OF ANOMALY EFFECTS IN FIELD DATA

We applied the evaluation of anomaly effects to a hydrogeological site-characterization study in the 8 km^2 Ammer floodplain close to Tübingen in Southwest Germany. Figure 5a shows the conceptual geological model as a vertical cross-section. We have identified four main sedimentary layers above the mudstone bedrock of the Upper Triassic Grabfeld-Formation in three drilling cores, namely from bottom to top: a clayey gravel layer on top of the bedrock, overlain by clay, calcareous sands, and alluvial fines. We observed the layer boundaries at similar depths over a distance of 400 m, indicating a predominantly horizontal layering. However, lithological features serving as relevant groundwater flow paths may be missed by the large spacing between the cores. For this, we measured an ERT profile along the core transect to detect potentially relevant features. In the following, we first compare a standard 2-D inversion of the ERT measurements to the evaluation of anomaly effects discussed above, to see whether our simplified approach is suitable to detect anomalies in the Ammer floodplain ERT measurements. More importantly, we determine a suitable electrode spacing from the ranges of anomaly effects to map the detected anomaly away from the ERT profile to determine the spatial extent and connectivity of the anomaly.

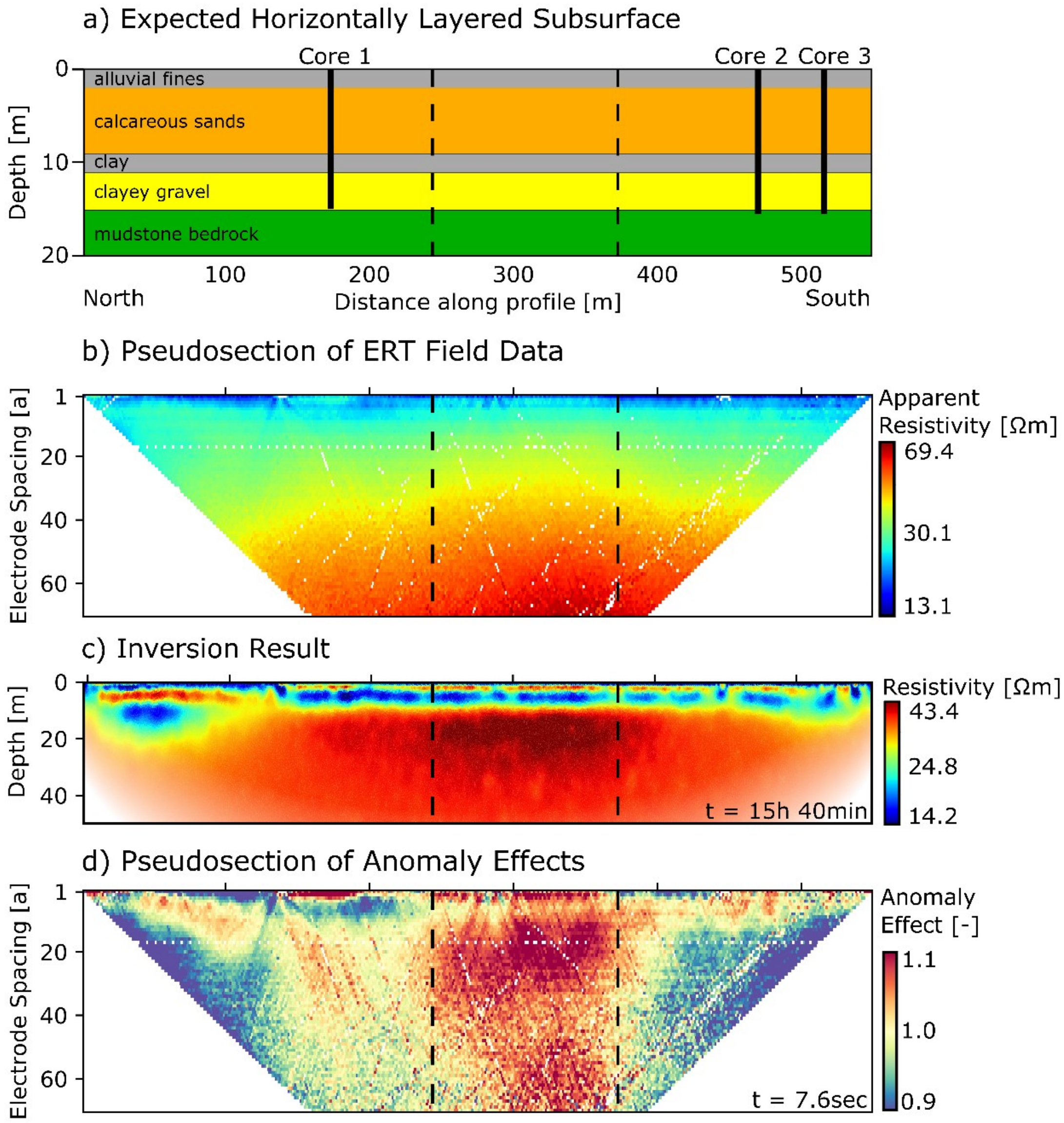

Figure 5: a) Horizontally layered conceptual geological model of the Ammer valley derived from three sediment cores. b) Manually cleaned Wenner-α data from a 550 m ERT profile with a = 1.5 m leading to c) an inversion result showing a higher resistive anomaly between 250 and 380 m in a depth of 10 - 30 m. d) The anomaly extent is also visible in the pseudosection of anomaly effects, calculated in a fraction of the time of the inversion.

1.5 column with color

4.1 Ammer floodplain ERT profile

We measured a 550 m long Wenner-α ERT profile with a RESECS acquisition system perpendicular to the main direction of the valley in order to validate the assumed horizontal layering and detect potential subsurface anomalies. For an estimated depth of investigation of $0.11 * \overline{AB} \approx 30\ m$, we chose an electrode spacing of $a = 1.5\ m$ and a maximum spacing of $70\ a$ (Roy and Apparao, 1971). Fieldwork consisted of 12 labor hours for setup, 12 hours of data acquisition, and 8 labor hours for dismantling.

We removed 2 measurements with more than 10% error as well as 369 individual outliers by manual picking before further data processing. The resulting data set *(17,934 measurements)*, visualized as a pseudosection in Figure 5b, shows relatively low values with an overall trend of increasing apparent resistivity with pseudodepth. A lateral inhomogeneity of relatively higher apparent resistivity can be inferred at ≈ 300 m along the profile, where no core information is available. We evaluated the data set by a standard ERT inversion using the software package pyBERT (Günther et al., 2006), shown in Figure 5c. We also computed anomaly effects for each data point according to the procedure outlined above and display the results in Figure 5d.

The inversion of the data set was performed with a homogeneous starting model to a maximum depth of 50 m. A maximum cell size of 1 m^2 led to an unstructured inversion mesh with 57,074 cells. We used the standard L2-Norm regularization with a smoothing factor of $\lambda = 20$ and a relative vertical weight of 0.7. The 2-D inversion took 15 h 40 min on a standard desktop computer. The resulting tomogram shows the general horizontal layering in the upper 10 m, which was in agreement with our prior knowledge of the site (Figure 5c). We ignored the higher-resistive region in the shallow zone left of core 1 and defined our target area between the cores 1 and 2. Here, a higher resistive anomaly is located between 250 and 380 m in the otherwise homogeneous bottom layer of highest resistivity. It is difficult to infer the thickness of the anomaly in the tomogram as the bottom contact is rather smooth.

The calculation of anomaly effects with a background apparent resistivity determined from the full, yet detrended data for each pseudodepth took 7.6 seconds. The resulting pseudosection of anomaly effects, displayed in Figure 5d, shows a region of strong positive anomaly effects between 250 and 380 m. Its lateral extent matches the extent of the anomaly visible in the inversion result, yet no interpretation of the true shape of the anomaly is possible.

This example demonstrates the enormous time saving in detecting anomalies and their lateral boundaries from an ERT data set. The inversion result may be interpreted in terms of resistivity values and depth allocation. However, the inevitable equivalence problem and smoothed anomaly boundaries require a final ground truthing for certainty. We can detect and delineate the anomaly similarly well based on the anomaly effects. Like in the interpretation of inversion results, a ground truthing is necessary to identify the type of anomaly and its true geometry.

Consequently, we drilled an additional core into the higher resistive anomaly to evaluate its relevance to the hydrogeology of the Ammer floodplain. From this core we could identify a thicker and cleaner gravel section with a five-meter deeper bedrock contact. We therefore interpreted the higher resistive anomaly as gravel filled paleo-channel incised into the mudstone bedrock and potentially functioning as a preferential flow path. The hydrogeological relevance of such a preferential flow path depends on its spatial extent and lateral continuity within the floodplain. It is therefore necessary to trace the gravel channel over large distances up- and downvalley from the ERT profile.

4.2 Spatial mapping with a fixed electrode spacing

Besides the time-efficiency, a main advantage of evaluating anomaly effects from the apparent resistivities is that it allows identifying pseudodepths and thus electrode spacings with a large range of anomaly effects. These electrode spacings are best suited for a geoelectric mapping campaign to delineate the spatial extent of the detected anomaly over many parallel investigation lines. The optimal spacings are site specific and account for the true subsurface parameter distribution, while the classical depth of measurement sensitivity estimates are based on the assumption of a horizontally layered subsurface.

We smoothed the anomaly effects for each pseudodepth with a Gaussian window of two standard deviations to suppress outliers. The resulting ranges of anomaly effects (RAE) are displayed in Figure 6a over the associated electrode spacings. The observed range of anomaly effects is the greatest for electrode spacings between 10 and 25 a, with a maximum at 15 a. We selected the corresponding electrode spacing of 22.5 m for a geoelectric mapping campaign to laterally trace the positive anomaly of the gravel-filled paleo-channel. The fieldwork included four people measuring the apparent resistivity at 738 locations along 10 profiles within 19 hours. The profile locations were limited to farm tracks and untilled agricultural fields, as well as by the floodplain boundary in the southwestern part of the study area. Along this boundary, the flat floodplain southwards transitions into gently sloping hillslopes mapped as bedrock in the regional geological map. We removed data with a measurement error >3 % and smoothed the remaining values using a moving average filter over 10 measurements along each profile to dampen outliers and represent the general trend. In general, the apparent resistivity values are comparable to those measured with the same electrode spacings in the ERT profile. Figure 6b shows an overview map of the floodplain study area with red and blue rectangles representing higher and lower apparent resistivities, respectively. Relatively higher apparent resistivities stretch in an approximately 150 m wide meandering belt from West to East, while measurements in the northern and southeastern part of the mapped area are relatively lower. Along the southwestern boundary of the floodplain we could not delineate the southern margin of the meandering belt as highest values of apparent resistivities allow no delineation comparable to other areas.

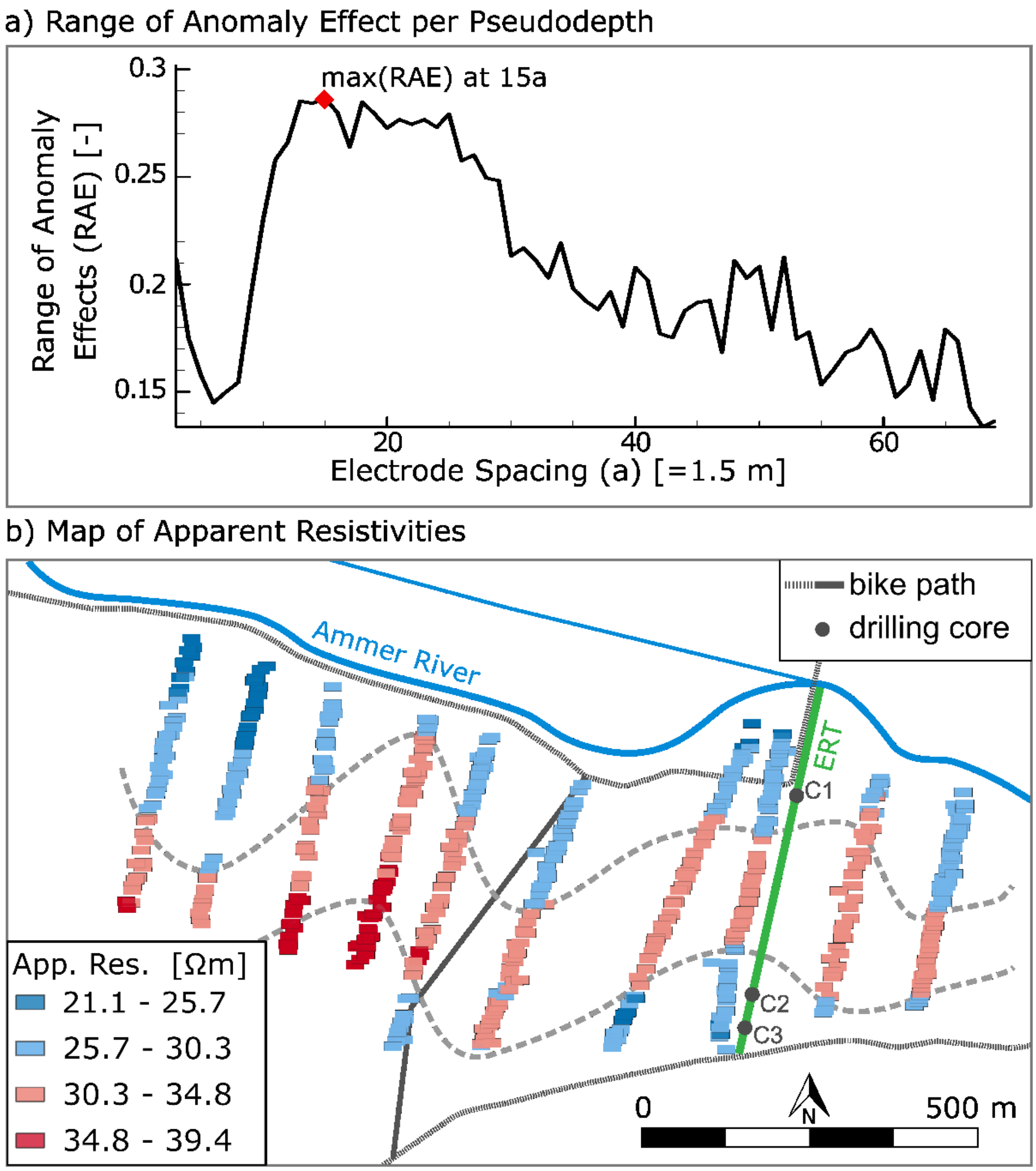

Figure 6: a) Range of anomaly effects per pseudodepth over the electrode spacing (a = 1.5 m) from the Ammer ERT data. Pseudodepths of 10-25 a show highest ranges of anomaly effects (maximum at 15 a), and are hence most suited for the subsequent lateral mapping with a fixed electrode spacing. b) Result of a mapping campaign with an electrode spacing of 15 a (22.5 m), indicating a meandering belt of higher resistivities in east-west direction.

1.5 column with color

We interpret the higher-resistive belt east of the bike path drawn solid as the lateral extent of the paleo-channel detected in the ERT data (Figure 6b). We also assume a continuous trace of the paleo-channel west of the bike path indicated by the grey dashed line. However, we interpret the lack of a southern delineation and the highest apparent resistivities in the area close to the southern floodplain boundary as evidence for the influence of other, higher resistive subsurface features such as a shallower bedrock. We therefore suggest an additional ERT profile along the bike path for ground truthing of the assumptions derived from the mapping results. Nevertheless, we could trace the higher resistive paleo-channel detected in the ERT data over at least 750 m within 19 hours, roughly the same amount of time as required to set up, measure, and break down the initial ERT profile.

4.3 Advantages of anomaly effects in field application

The lateral extent of the higher-resistive anomaly is similar in the inversion result and the pseudosection of anomaly effects (Figure 5c and d), but the inversion yields more reliable information on a probable resistivity distribution in the subsurface. It therefore serves as a reference for the potential depth, thickness and parameter distribution of the resistivity anomaly at the profile location. However, the pseudosection of anomaly effects can be used to determine suitable electrode spacings for a subsequent spatial mapping of the anomaly at places different from the initial ERT profile. One or several electrode spacings with a large range of anomaly effects may be used for a targeted mapping campaign covering 100,000s of m^2 without the need of another ERT profile. In the Ammer floodplain, we mapped an area of more than 600,000 m^2 within 19 hours, traced the target anomaly over at least 750 m and defined a suitable location for an additional ERT profile. Capacitive geoelectric mapping or pulled array continuous electrical profiling tools could greatly increase the mapping speed and therefore the efficiency of the preliminary site characterization.

5 CONCLUSIONS

Geoelectric mapping is an efficient method to trace the lateral extent of a resistivity anomaly over large areas. We use our evaluation of anomaly effects to detect an anomaly in data space of a preliminary ERT profile and determine a site-specific electrode configuration for a subsequent spatial mapping. We have presented two approaches to calculate the background apparent resistivity at each location, by either analyzing the full profile of ERT data within the same pseudodepth, or a subset thereof centered about the investigation point. The latter approach is suitable to separate effects of lateral trends in the background apparent resistivity from those of the targeted anomaly. The pseudosection of anomaly effects then visualizes the lateral extents of the anomaly, which may be confirmed by a full inversion of the data.

More importantly, we can determine the range of anomaly effects for each pseudodepth. Electrode spacings with high ranges of anomaly effects are sensitive to lateral resistivity changes in the subsurface and independent of standard depth of measurement sensitivity estimates. The range of anomaly effects therefore serves as a site-specific measure for suitable configurations for geoelectric mapping with constant electrode spacing. We tested this method at our floodplain field site in Southwest Germany. Ranges of anomaly effects from a preliminary Wenner-α ERT data set helped identifying an optimal electrode spacing for subsequent mapping. With the latter, we could trace an interpreted paleo-channel resistivity anomaly away from a preliminary ERT profile. The map of measured apparent resistivities hereby reveals a meandering course of the channel structure throughout the floodplain and helps guiding future investigations and well installations. The initial ERT profile required 20 labor hours of field work and 12 hours of data acquisition, whereas a mapping profile of similar length was measured within 4 labor hours. In fact, the mapping campaign covered an area of more than 600,000 m^2 in the time required to set up, measure, and break down the initial ERT profile. This time advantage scales with the area of investigation and the required separation of survey lines.

The proposed method does not replace a careful inversion of available full ERT data sets. In fact, the target feature is determined from the inversion result of a preliminary full ERT dataset. The evaluation of ranges of anomaly effects rather serves as a tool to determine suitable electrode spacings for a site-specific, targeted mapping campaign. Once detected, an anomaly can be laterally traced over large, flat areas to help guide subsequent more thorough investigations. Time savings compared to parallel full 2-D ERT profiles hereby apply to fieldwork and data acquisition (single representative profile and mapping vs. several full profiles), as well as data evaluation (seconds of anomaly effect calculation vs. hours of inversion).

6 DATA AVAILABILITY

Datasets and codes related to this article can be found at http://hdl.handle.net/10900.1/8e00cb6d-fa76-44d1-b148-203a14a67625 (2020).

7 ACKNOWLEDGEMENT

This work was supported by the Collaborative Research Center 1253 CAMPOS (Project 3: Floodplain Hydrology), funded by the German Research Foundation (DFG, Grant Agreement SFB 1253/1 2017). We want to thank T. Günther for his constant help with pyBERT and K. Singha for her insightful comments on this manuscript.

8 REFERENCES

Aizebeokhai, A. P., and A. I. Olayinka, 2011, Anomaly effects of orthogonal paired-arrays for 3D geoelectrical resistivity imaging: Environmental Earth Sciences, **64**, 2141–2149, doi: 10.1007/s12665-011-1041-9.

Akca, İ., Ç. Balkaya, A. Pülz, H. S. Alanyalı, and M. A. Kaya, 2019, Integrated geophysical investigations to reconstruct the archaeological features in the episcopal district of Side (Antalya, Southern Turkey): Journal of Applied Geophysics, **163**, 22–30.

Amini, A., and H. Ramazi, 2016, Anomaly enhancement in 2D electrical resistivity imaging method using a residual resistivity technique: Journal of the Southern African Institute of Mining and Metallurgy, **116**, doi: 10.17159/2411-9717/2016/v116n2a7.

Apparao, A., T. G. Rao, R. S. Sastry, and V. S. Sarma, 1992, Depth of detection of buried conductive targets with different electrode arrays in resistivity prospecting: Geophysical Prospecting, **40**, 749–760, doi: 10.1111/j.1365-2478.1992.tb00550.x.

Barker, R. D., 1989, Depth of investigation of collinear symmetrical four-electrode arrays: GEOPHYSICS, **54**, 1031–1037.

Bentley, L. R., and M. Gharibi, 2004, Two- and three-dimensional electrical resistivity imaging at a heterogeneous remediation site: GEOPHYSICS, **69**, 674–680.

Bhattacharya, B. B., and M. K. Sen, 1981, Depth of investigation of collinear electrode arrays over homogeneous anisotropic half-space in direct current methods: GEOPHYSICS, **46**, 768–780.

Carpenter, E. W., 1955, SOME NOTES CONCERNING THE WENNER CONFIGURATION: Geophysical Prospecting, **3**, 388–402.

Cartwright, K., and M. R. McComas, 1968, Geophysical Surveys in the Vicinity of Sanitary Landfills in Northeastern Illinoisa: Ground Water, **6**, 23–30.

Chambers, J. E., O. Kuras, P. I. Meldrum, R. D. Ogilvy, and J. Hollands, 2006, Electrical resistivity tomography applied to geologic, hydrogeologic, and engineering investigations at a former waste-disposal site: Environmental Geology, **71**, B231-B239.

Chambers, R., Ogilvy O., and Kuras J. C. J., 2002, 3D electrical imaging of known targets at a controlled environmental test site: Environmental Geology, **41**, 690–704.

Christiansen, A. V., and E. Auken, 2012, A global measure for depth of investigation: GEOPHYSICS, **77**, no. 4, WB171-WB177, doi: 10.1190/GEO2011-0393.1.

Dahlin, T., and M. H. Loke, 1997, Quasi-3D resistivity imaging - mapping of three dimensional structures using two dimensional DC resistivity techniques, *in,* 3rd EEGS Meeting: EAGE Publications BVNetherlands.

Dahlin, T., and B. Zhou, 2004, A numerical comparison of 2D resistivity imaging with 10 electrode arrays: Geophysical Prospecting, **52**, 379–398, doi: 10.1111/j.1365-2478.2004.00423.x.

Day-Lewis, F. D., 2005, Applying petrophysical models to radar travel time and electrical resistivity tomograms: Resolution-dependent limitations: Journal of Geophysical Research, **110**, 277.

Demirel, S., D. Roubinet, J. Irving, and E. Voytek, 2018, Characterizing Near-Surface Fractured-Rock Aquifers: Insights Provided by the Numerical Analysis of Electrical Resistivity Experiments: Water, **10**, 1117, doi: 10.3390/w10091117.

Domenico, D. de, F. Giannino, G. Leucci, and C. Bottari, 2006, Integrated geophysical surveys at the archaeological site of Tindari (Sicily, Italy): Journal of Archaeological Science, **33**, 961–970.

Edwards, L. S., 1977, A MODIFIED PSEUDOSECTION FOR RESISTIVITY AND IP: GEOPHYSICS, **42**, 1020–1036.

Evjen, H. M., 1938, DEPTH FACTORS AND RESOLVING POWER OF ELECTRICAL MEASUREMENTS: GEOPHYSICS, **3**, 78–95.

Frohlich, R. K., D. W. Urish, J. Fuller, and M. O'Reilly, 1994, Use of geoelectrical methods in groundwater pollution surveys in a coastal environment: Journal of Applied Geophysics, **32**, 139–154.

Gonzales Amaya, A., T. Dahlin, G. Barmen, and J.-E. Rosberg, 2016, Electrical Resistivity Tomography and Induced Polarization for Mapping the Subsurface of Alluvial Fans: A Case Study in Punata (Bolivia): Geosciences, **6**, 51.

Greenfield, R. J., 1979, Review of Geophysical Approaches to the Detection of Karst: Environmental & Engineering Geoscience, **xvi**, 393–408.

Günther, T., C. Rücker, and K. Spitzer, 2006, Three-dimensional modelling and inversion of dc resistivity data incorporating topography - II. Inversion: Geophysical Journal International, **166**, 506–517.

Hauquin, T., and Q. Mourey, 2019, The detection of old masonry tunnels as low electrical resistivity anomalies-application to one covered stream tunnel of the Cevennes Mountain region (France): Journal of Applied Geophysics, **168**, 12–23.

Hennig, T., A. Weller, and M. Möller, 2008, Object orientated focussing of geoelectrical multielectrode measurements: Journal of Applied Geophysics, **65**, 57–64.

Kelly, W. E., 1976, Geoelectric Sounding for Delineating Ground-Water Contamination: Ground Water, **14**, 6–10.

Khaki, M., I. Yusoff, N. Islami, and S. Saboohi, 2016, Integrated geoelectrical and hydrogeochemical investigation for mapping the aquifer at Langat Basin, Malaysia: Environmental Earth Sciences, **75**, 189.

Klefstad, G., L. V. A. Sendlein, and R. C. Palmquist, 1977, Limitations of the Electrical Resistivity Method in Landfill Investigations: Ground Water, **15**, 418–427.

[dataset] Klingler, S., C. Leven, O. A. Cirpka, and P. Dietrich, 2020, Anomaly effect-driven optimization of direct-current geoelectric mapping surveys in large areas: Datasets and Supplementary Materials, http://hdl.handle.net/10900.1/8e00cb6d-fa76-44d1-b148-203a14a67625.

Knudby, C., and J. Carrera, 2005, On the relationship between indicators of geostatistical, flow and transport connectivity: Advances in Water Resources, **28**, 405–421.

Loke, M. H., P. B. Wilkinson, and J. E. Chambers, 2010, Fast computation of optimized electrode arrays for 2D resistivity surveys: Computers & Geosciences, **36**, 1414–1426, doi: 10.1016/j.cageo.2010.03.016.

Martin, J. M., M. E. Everett, and P. S.K. Knappett, 2019, ERT INVESTIGATION OF AN ANTECEDENT FLOODPLAIN CHANNEL-BELT, *in* D. Mills, ed., Symposium on the Application of Geophysics to Engineering and Environmental Problems 2019: Society of Exploration Geophysicists and Environment and Engineering Geophysical Society, 97–100.

Maurya, P. K., V. K. Rønde, G. Fiandaca, N. Balbarini, E. Auken, P. L. Bjerg, and A. V. Christiansen, 2017, Detailed landfill leachate plume mapping using 2D and 3D electrical resistivity tomography - with correlation to ionic strength measured in screens: Journal of Applied Geophysics, **138**, 1–8.

Militzer, H., R. Rösler, and W. Lösch, 1979, Theoretical and experimental investigations for cavity research with geoelectrical resistivity methods: Geophysical Prospecting, **27**, 640–652, doi: 10.1111/j.1365-2478.1979.tb00991.x.

Moník, M., Z. Lenďáková, J. J. Ibáñez, J. Muñiz, F. Borell, E. Iriarte, L. Teira, and F. Kuda, 2018, Revealing early villages - Pseudo-3D ERT geophysical survey at the pre-pottery Neolithic site of Kharaysin, Jordan: Archaeological Prospection, **25**, 339–346.

Naudet, V., A. Revil, E. Rizzo, J.-Y. Bottero, and P. Bégassat, 2004, Groundwater redox conditions and conductivity in a contaminant plume from geoelectrical investigations: Hydrology and Earth System Sciences, **8**, 8–22.

Negri, S., G. Leucci, and F. Mazzone, 2008, High resolution 3D ERT to help GPR data interpretation for researching archaeological items in a geologically complex subsurface: Journal of Applied Geophysics, **65**, 111–120.

Oldenburg, D. W., and Y. Li, 1999, Estimating depth of investigation in dc resistivity and IP surveys: GEOPHYSICS, **64**, 403–416.

Renard, P., and D. Allard, 2013, Connectivity metrics for subsurface flow and transport: Advances in Water Resources, **51**, 168–196.

Roy, A., and A. Apparao, 1971, DEPTH OF INVESTIGATION IN DIRECT CURRENT METHODS: GEOPHYSICS, **36**, 943–959.

Roy, A., and R. L. Dhar, 1971, RADIUS OF INVESTIGATION IN DC RESISTIVITY WELL LOGGING: GEOPHYSICS, **36**, 754–760.

Rücker, C., T. Günther, and K. Spitzer, 2006, Three-dimensional modelling and inversion of dc resistivity data incorporating topography - I. Modelling: Geophysical Journal International, **166**, 495–505.

Rücker, C., T. Günther, and F. M. Wagner, 2017, pyGIMLi: An open-source library for modelling and inversion in geophysics: Computers & Geosciences, **109**, 106–123, doi: 10.1016/j.cageo.2017.07.011.

Sahbi, H., D. Jongmans, and R. Charlier, 1997, Theoretical study of slope effects in resistivity surveys and applications: Geophysical Prospecting, **45**, 795–808, doi: 10.1046/j.1365-2478.1997.580297.x.

Sinha, R., G. S. Yadav, S. Gupta, A. Singh, and S. K. Lahiri, 2013, Geo-electric resistivity evidence for subsurface palaeochannel systems adjacent to Harappan sites in northwest India: Quaternary International, **308-309**, 66–75.

Sørensen, K. I., E. Auken, N. B. Christensen, and L. Pellerin, 2005, 21. An Integrated Approach for Hydrogeophysical Investigations: New Technologies and a Case History, *in* D. K. Butler, ed., Near-surface geophysics: Society of Exploration Geophysicists, 585–606.

Stummer, P., H. Maurer, and A. G. Green, 2004, Experimental design: Electrical resistivity data sets that provide optimum subsurface information: GEOPHYSICS, **69**, 120–139, doi: 10.1190/1.1649381.

Szalai, S., A. Novák, and L. Szarka, 2011, Which geoelectric array sees the deepest in a noisy environment? Depth of detectability values of multielectrode systems for various two-dimensional models: Physics and Chemistry of the Earth, Parts A/B/C, **36**, 1398–1404, doi: 10.1016/j.pce.2011.01.008.

Trinchero, P., X. Sánchez-Vila, and D. Fernàndez-Garcia, 2008, Point-to-point connectivity, an abstract concept or a key issue for risk assessment studies?: Advances in Water Resources, **31**, 1742–1753.

Tsokas, G. N., P. I. Tsourlos, A. Stampolidis, d. Katsonopoulou, and S. Soter, 2009, Tracing a major Roman road in the area of ancient Helike by resistivity tomography: Archaeological Prospection, **16**, 251–266.

Uhlemann, S., O. Kuras, L. A. Richards, E. Naden, and D. A. Polya, 2017, Electrical resistivity tomography determines the spatial distribution of clay layer thickness and aquifer vulnerability, Kandal Province, Cambodia: Journal of Asian Earth Sciences, **147**, 402–414.

Uhlemann, S., P. B. Wilkinson, H. Maurer, F. M. Wagner, T. C. Johnson, and J. E. Chambers, 2018, Optimized survey design for electrical resistivity tomography: combined optimization of measurement configuration and electrode placement: Geophysical Journal International, **214**, 108–121, doi: 10.1093/gji/ggy128.

Urish, D. W., 1983, The Practical Application of Surface Electrical Resistivity to Detection of Ground-Water Pollution: Ground Water, **21**, 144–152.

van Nostrand, R. G., 1953, Limitations on resistivity methods as inferred from the buried sphere problem: GEOPHYSICS, **18**, 423–433, doi: 10.1190/1.1437895.

Walker, J. P., and P. R. Houser, 2002, Evaluation of the OhmMapper Instrument for Soil Moisture Measurement: Soil Science Society of America Journal, **66**, 728–734, doi: 10.2136/sssaj2002.0728.

Warner, D. L., 1969, Preliminary Field Studies Using Earth Resistivity Measurements for Delineating Zones of Contaminated Ground Water: Ground Water, **7**, 9–16.

Wienhöfer, J., and E. Zehe, 2014, Predicting subsurface stormflow response of a forested hillslope – the role of connected flow paths: Hydrology and Earth System Sciences, **18**, 121–138.

Wilkinson, P. B., P. I. Meldrum, J. E. Chambers, O. Kuras, and R. D. Ogilvy, 2006, Improved strategies for the automatic selection of optimized sets of electrical resistivity tomography measurement configurations: Geophysical Journal International, **167**, 1119–1126, doi: 10.1111/j.1365-246X.2006.03196.x.

Worthington, P. F., and R. D. Barker, 1977, Detection of disused vertical mineshafts at shallow depths by geoelectrical methods: Geoexploration, **15**, 111–120.

Zhou, B., and T. Dahlin, 2003, Properties and effects of measurement errors on 2D resistivity imaging surveying: Near Surface Geophysics, **1**, 105–117.